Letter Vol. 47, No. 22 / 15 November 2022 / Optics Letters 5789

Stress-induced birefringence in 3D direct laser written micro-optics

Michael Schmid* and Harald Giessen

4th Physics Institute and Research Center SCoPE, University of Stuttgart, Pfaffenwaldring 57, 70569 Stuttgart, Germany
**Corresponding author: m.schmid@pi4.uni-stuttgart.de*

Received 26 September 2022; revised 15 October 2022; accepted 17 October 2022; posted 17 October 2022; published 2 November 2022

3D direct laser writing is a widely used technology to create different nano- and micro-optical devices for various purposes. However, one big issue is the shrinking of the structures during polymerization, which results in deviations from the design and in internal stress. While the deviations can be compensated by adapting the design, the internal stress remains and induces birefringence. In this Letter, we successfully demonstrate the quantitative analysis of stress-induced birefringence in 3D direct laser written structures. After presenting the measurement setup based on a rotating polarizer and an elliptical analyzer, we characterize the birefringence of different structures and writing modes. We further investigate different photoresists and the implications for 3D direct laser written optics.

https://doi.org/10.1364/OL.476464

Over the last decade, 3D direct laser writing has advanced to become a widely used tool to create complex micro-optics for various purposes. Different scientific fields, such as biology [1,2], microfluidics [3], sensing [4,5], endoscopy [6,7], imaging [8], and beam shaping [9,10], benefit from the huge design freedom and versatility.

In all of these applications, one needs to reduce aberrations to achieve the best possible optical performance. Using the design freedom of 3D direct laser writing, monochromatic aberrations can easily be reduced by the use of aspheric surfaces or multi-lens objectives [11]. Even chromatic aberrations can be corrected with a combination of photoresists with different dispersions, or a combination of diffractive and refractive surfaces [12,13].

All of these aberration reductions are based on the assumption that the light travels through the material of the optical structure as a perfect wavefront without any distortions. This would be true for an ideal isotropic and homogeneous material but, owing to shrinking during the writing process [14], stress is induced in the material, which leads to birefringence, as is well known from other polymers [15].

Owing to the stress, and therefore loss, of physical isotropy, the polymer's permittivity tensor also becomes anisotropic, resulting in slightly different refractive indices, depending on the polarization and propagation direction of the light. This leads to an effective path length difference and a change in the polarization state, depending on the material thickness [Fig. 1(a)]. Birefringence is defined as the difference in the refractive indices $\Delta n = n_e - n_o$. When light travels through a birefringent material of thickness d, this results in a difference of optical phase shift, called retardance, of $\Delta = \Delta n \cdot d$.

To measure the retardance, we use a setup based on the work of Oldenbourg [16,17], although other setups are possible [18]. We use collimated monochromatic (650 nm) incident light, which passes through a rotating linear polarizer at 0°, 45°, 90°, and 135°. The original measurement setup uses two liquid crystal retarders to create incident light with adjustable ellipticity, to increase the sensitivity of the system. With the condenser, the light is guided through the sample and imaged with the objective. The circular analyzer consists of a $\lambda/4$ plate at 45° and a linear polarizer at 0° [Fig. 1(b)]. The measured intensity can be calculated using the Jones formalism for the four incident polarizations, resulting in $I_{1/2} = 0.5\, I_0[1 \pm \sin 2\phi \sin \Delta]$ and $I_{3/4} = 0.5\, I_0[1 \pm \cos 2\phi \sin \Delta]$, where I_0 is the distribution of the illumination intensity on the sample. Defining $A = (I_1 - I_2)/(I_1 + I_2)$ and $B = (I_4 - I_3)/(I_4 + I_3)$, the retardance value Δ and slow axis angle ϕ can be calculated as

$$\Delta = 2\tan^{-1}\left(\frac{\sqrt{A^2 + B^2}}{1 + (1 - \sqrt{A^2 + B^2}}\right), \tag{1}$$

$$\phi = \frac{1}{2}\tan^{-1}\left(\frac{A}{B}\right). \tag{2}$$

We can use the retardance measurements to make structural features visible that cannot be seen otherwise and investigate whether the retardance is strong enough to interfere with the imaging quality. In Fig. 2(a), a 30° tilted microscope image of a shell/scaffold-written, 150-µm high IP-S half sphere is depicted, with the scaffold structure scarcely visible. However, between crossed polarizers, one can clearly see the support structures [Fig. 2(b)]. We fabricated the lens using a NanoScribe Professional GT (NanoScribe GmbH) with a 25× Zeiss objective. The writing parameters are: laser power, 70%; scan speed, 50 mm/s; slicing, 0.2 µm; hatching, 0.5 µm. We use a shell/scaffold mode with a contour count of 15 lines and a base count of 20 lines. The scaffold has a wall spacing of 20 µm and a floor spacing of 25 µm, with slice counts of 1.

According to the equation, the measuring process involves four individual measurements [Figs. 2(c) to 2(f)], with the four different linear incident polarizations 0°, 45°, 90°, and 135°, to measure I_{1-4}.

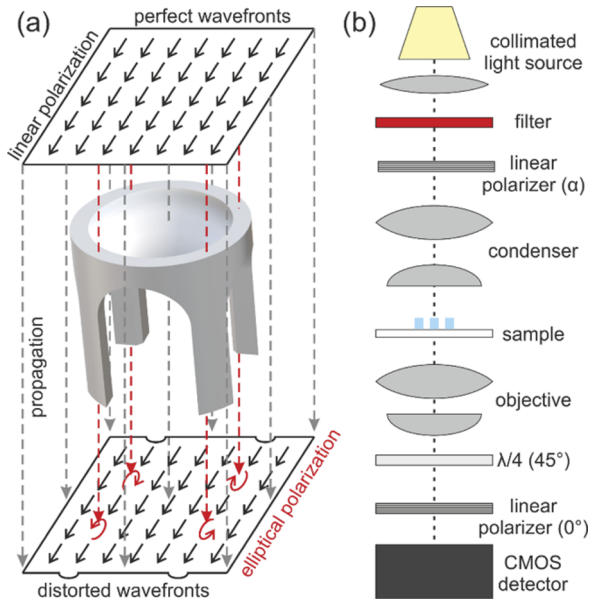

Fig. 1. (a) Distortion of a perfect wavefront after traveling through a 3D printed structure. Linearly polarized incident light changes to elliptical polarization, depending on the birefringence. (b) Measurement principle with collimated light source, monochromatic filter at 650 nm, rotating linear polarizer, condenser, sample, imaging objective, and circular analyzer consisting of $\lambda/4$ plate and linear polarizer.

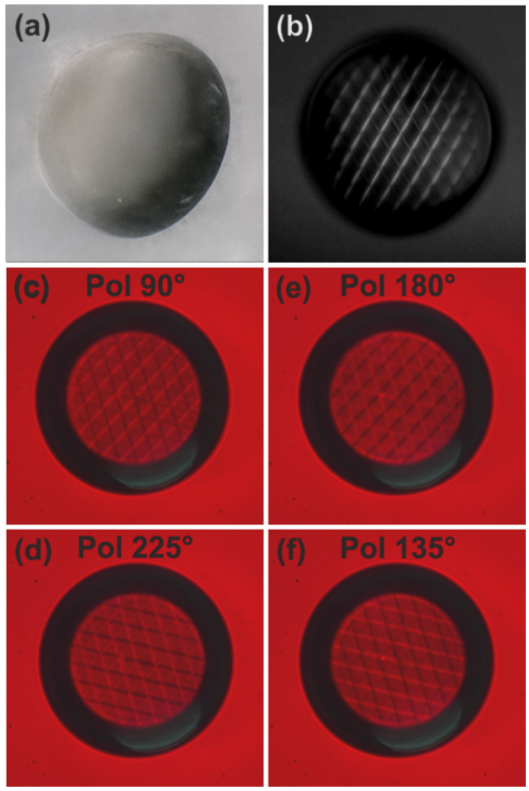

Fig. 2. (a) 30° tilted micrograph of 150-µm high 3D printed IP-S half sphere in shell/scaffold mode with a diameter of 300 µm. (b) Top picture with sample between crossed polarizers, exhibiting internal structures owing to birefringence that are scarcely visible in the micrograph. (c)–(f) Images with different angles of linear polarizer (90°, 180°, 225°, and 135°), necessary for the retardance calculation.

In the images with different illumination polarization, the different parts of the scaffold can be clearly seen. Depending on the orientation of the scaffold and the resulting stress birefringence relative to the polarization direction, the different line segments appear darker and brighter in the different images. The dark arc around the lenses appears as a result of total internal reflection.

For the retardance calculations, it is crucial that the sample does not move during the measurement; otherwise, the calculations will not be correct. The calculations are made for each pixel separately and give the corresponding retardance and orientation of the slow axis. In Figs. 3(a) and 3(b), the calculated slow axis orientation (in degrees relative to the vertical) and the retardance (in λ) are depicted. Both values can be combined in a cone plot [Fig. 3(c)], where the color map indicates the retardance and the cones point into the direction of the slow axis orientation. As expected, the birefringence is highest along the scaffold structure and reaches values above $\lambda/20$ or 40 nm. Dividing by the height of the half sphere in the middle of 150 µm, this results in a retardance of 0.4λ/mm or $\Delta n = 2.6 \times 10^{-4}$. The slow axis orientation always points toward the scaffold segments. Figure 3(d) reveals the effect of post-treatment on the birefringence induced by the scaffold. The sample was put on a hotplate at 100°C for 2 h. The slow axis orientation does not change, but the retardance decreases by about 30%. Longer heat treatment, as well as additional UV treatment, did not reduce the retardance any further. Also, UV treatment before putting the sample on the hotplate did not have any measurable effect on the retardance. We also performed the post-treatment on other structures written in normal full writing mode, where the effect on the retardance was much smaller and could be neglected.

This analysis clearly reveals subtle differences between two-photon (scaffold) and one-photon (in between the structures) polymerized photopolymers. Not only is there a slight refractive index difference, which can be annealed by post-treatment by heating, but the writing direction of two-photon polymerization seems to result in additional uniaxial properties along the writing direction.

Figure 4 depicts the results of retardance measurements of different IP-S test structures. Figures 4(a) and 4(b) are micrographs of two 150-µm high IP-S cubes, one with holes to induce more stress. Figures 4(c) and 4(d) show the slow axis orientation along the edges of the cube and around the corners. The holes induce additional stress and therefore retardance between them. This is also visible in Figs. 4(e) and 4(f), together with the corresponding retardance values. The retardance reaches values up to $\lambda/20$ near the edges and around the holes. We also investigate the birefringence of a 150-µm high half sphere [Fig. 4(g)], with retardance values below $\lambda/50$. Furthermore, we measure the retardance of a 300-µm high shell/scaffold-written half sphere [Fig. 4(h)], exhibiting retardances over $\lambda/10$, around twice the value of the 150-µm high shell/scaffold half sphere (Fig. 3).

This is expected, as the retardance should increase linearly with the object height, as long as the local stress remains the same. To further investigate the stress-induced birefringence, we also use another photoresist, namely IP-Visio, which is known for better transparency but exhibits stronger shrinkage and delamination issues [19].

Figure 5 depicts 300-µm high IP-Visio cubes fabricated with different writing parameters between two crossed polarizers and retardance measurements of the same structures. With lower

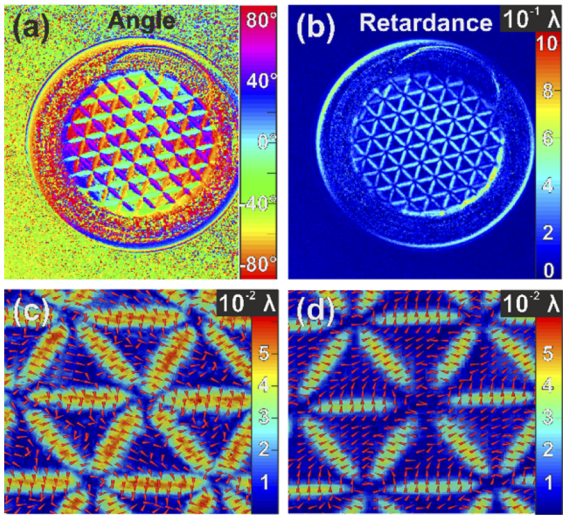

Fig. 3. (a) Calculated slow axis orientation ϕ (°) and (b) value of measured retardance Δ (in units of $10^{-1}\lambda$) of IP-S shell/scaffold-written half sphere (height 150 µm, diameter 300 µm). (c) Close-up retardance cone plot, combining the values and direction of (a) and (b). In the supporting structures, the retardance reaches values above $\lambda/20$ (40 nm) along the structures. Divided by the height of 150 µm this results in 0.4λ/mm or $\Delta n = 2.6 \times 10^{-4}$. (d) After 2 h of heat treatment on a hotplate at 100°C, the retardance values (in units of $10^{-2}\lambda$) decrease by about 30%.

effective writing intensity, delamination from the substrate at the structure edges increased, resulting in retardance values up to $\lambda/5$ (130 nm). Divided by the height, 300 µm, this resulted in 0.66λ/mm or $\Delta n = 4.3 \times 10^{-4}$, 1.7 times the birefringence of the IP-S structures. We tried to increase the adhesion of the photoresist by oxygen plasma treatment (10 min) before applying it to the substrate, however, without noticeable improvement. Unfortunately, another approach by spin-coating a thin layer of SU-8 onto the substrate also did not improve the adhesion. The only approach that worked was to increase the effective writing dose (here, smaller slicing distances), which increases the writing time of the structures.

Other 300-µm high 3D written structures of IP-Visio, such as a cylinder [Fig. 6(a)] also exhibit delamination and thus retardances up to $\lambda/5$ at the edges; this drastically decreases with a smaller slicing [Figs. 6(c) and 6(d)]. However, a 300-µm high half sphere does not show delamination at the edges, even with a slicing of 1 µm, and exhibits comparably small retardance values below $\lambda/50$ [Fig. 6(e)]. Figure 6(b) depicts a typical singlet lens, which is printed onto four legs. The 300-µm high legs induce retardances up to 0.08λ, but the retardance does not appear inside the lens, which exhibits low retardances up to $\lambda/50$ [Fig. 6(h)]. This means that both the 300-µm high half sphere and the singlet lens on legs do not exhibit stress-induced birefringence, which should thus not reduce the imaging quality. Sophisticated development protocols may reduce the shrinkage and thus the delamination as well as internal stress [20]. The investigated methacrylate-based photoresists IP-S and IP-Visio both exhibit shrinkage and thus stress during the fabrication process, typical for 3D direct laser written photoresists. Mechanical properties of the photoresists influence the exhibited stress–strain relation, but are quite similar to other used resins, such as IP-Dip, Ormo-Comp, or SU-8 [21]. Thus our results are also beneficial for

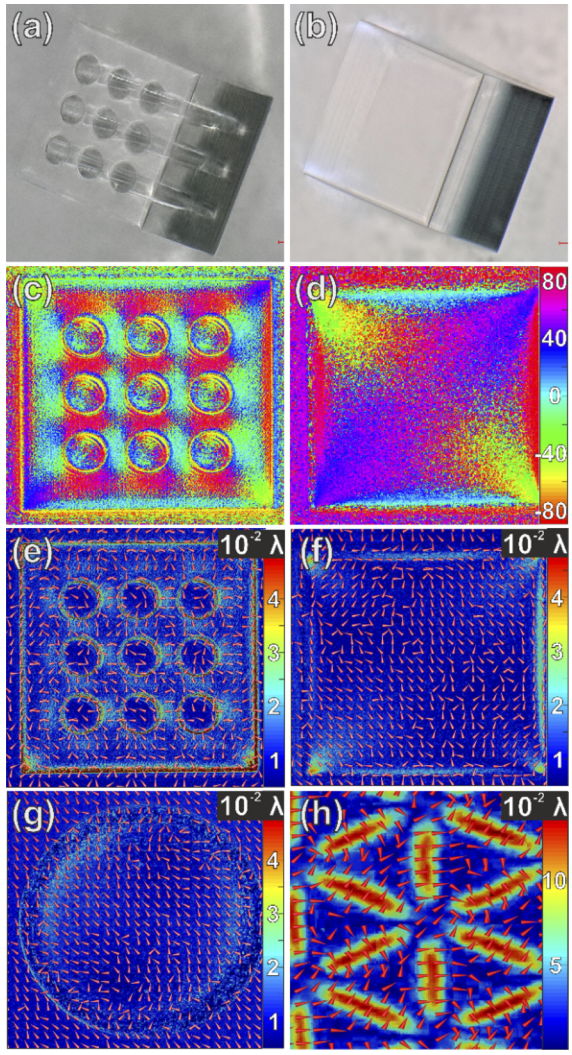

Fig. 4. (a), (b) 30° tilted micrographs of 150-µm high IP-S cube (side length 150 µm): (a) with holes and (b) without holes. (c), (d) Slow axis orientation. (e), (f) Corresponding retardance value and cone plots. The retardance reaches values up to $\lambda/20$ orientated along the edges and toward the holes. (g) Retardance measurement of a 150-µm high half sphere (diameter 300 µm) with retardance below $\lambda/50$. (h) 300-µm high shell/scaffold half sphere exhibiting retardance over $\lambda/10$, around twice the value of the 150-µm high half sphere depicted in Fig. 3.

other materials beyond IP resins and provide a first indication of expected retardance values.

In summary, we demonstrated a measurement setup utilizing a rotating polarizer and a circular analyzer to perform retardance measurements on 3D written structures. We investigate different test structures made of IP-S and IP-Visio. As expected, the stress and birefringence is strongest around the edges of the structures. It is also very prominent in the shell/scaffold writing mode and when delamination of the substrate occurs. For typical half spheres and singlet lenses on legs, the retardance values are low and should not interfere with the imaging performance. However, for structures thicker than 500 µm, especially written in shell/scaffold mode or exhibiting delamination, the retardance can become relevant.

Funding. European Research Council (3DPRINTEDOPTICS, COM-

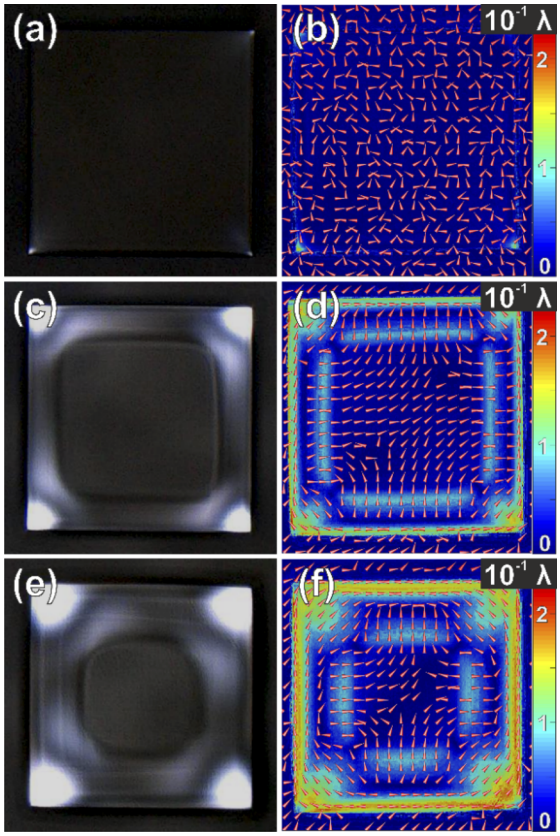

Fig. 5. (Left) 300-µm high IP-Visio cubes (side length 300 µm) between crossed polarizers; (right) retardance measurements (in units of λ): (a), (b) slicing 0.2 µm; (c), (d) slicing 1 µm; (e), (f) slicing 2 µm. The laser power was always 100% and the scan speed was set to 75 mm/s. With lower effective writing intensity, delamination from the substrate at the structure edges increases, resulting in stronger stress and therefore retardance up to $\lambda/5$ (130 nm). Divided by the height, 300 µm, this results in 0.66λ/mm or $\Delta n = 4.3 \times 10^{-4}$.

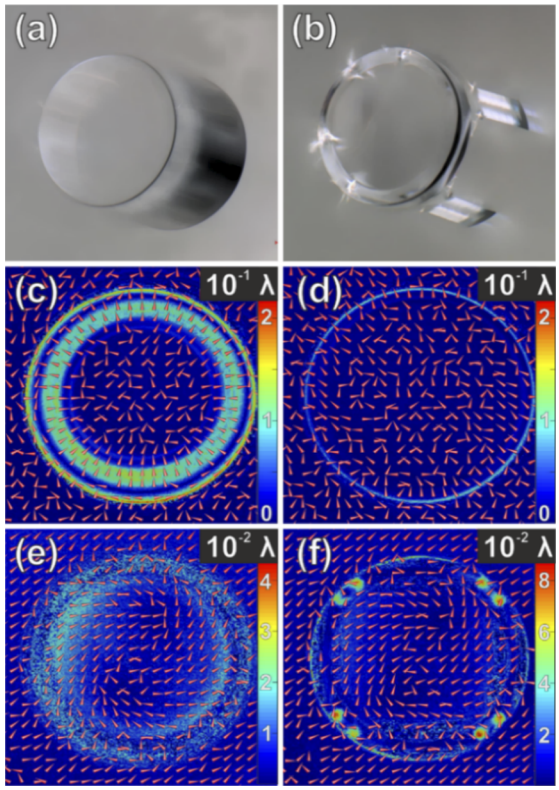

Fig. 6. 30° micrographs of (a) 300-µm high IP-Visio cylinder and (b) singlet lens on legs with 300 µm diameter. (c), (d) Retardance measurement (in units of 10^{-1} and $10^{-2}\lambda$) of cylinder with (c) 1-µm slicing and (d) 0.2-µm slicing. (e) 300 µm high half-sphere (diameter 600 µm) and (f) singlet lens on legs with 0.2-µm slicing. All with laser power 100% and scan speed 50 mm/s.

PLEXPLAS); Baden-Württemberg Stiftung (OPTERIAL); Bundesministerium für Bildung und Forschung (13N10146, PRINTFUNCTION, PRINTOPTICS); Deutsche Forschungsgemeinschaft (GRK 2642).

Disclosures. The authors declare no conflicts of interest.

Data availability. Data underlying the results presented in this Letter are not publicly available at this time but may be obtained from the authors upon reasonable request.

REFERENCES

1. H. Eto, H. G. Franquelim, M. Heymann, and P. Schwille, Soft Matter **17**, 5456 (2021).
2. A. Selimis, V. Mironov, and M. Farsari, Microelectron. Eng. **132**, 83 (2015).
3. R. K. Jayne, MÇ Karakan, K. Zhang, N. Pierce, C. Michas, D. J. Bishop, C. S. Chen, K. L. Ekinci, and A. E. White, Lab Chip **21**, 1724 (2021).
4. A. Toulouse, J. Drozella, S. Thiele, H. Giessen, A. Herkommer, A. Toulouse, J. Drozella, S. Thiele, H. Giessen, and A. Herkommer, Light Adv. Manuf. **2**, 20 (2021).
5. P. Dietrich, G. Göring, M. Trappen, M. Blaicher, W. Freude, T. Schimmel, H. Hölscher, and C. Koos, Small **16**, 1904695 (2020).
6. J. Li, S. Thiele, B. C. Quirk, R. W. Kirk, J. W. Verjans, E. Akers, C. A. Bursill, S. J. Nicholls, A. M. Herkommer, H. Giessen, and R. A. McLaughlin, Light: Sci. Appl. **9**, 124 (2020).
7. F. Akhoundi, Y. Qin, N. Peyghambarian, J. K. Barton, and K. Kieu, Biomed. Opt. Express **9**, 2326 (2018).
8. S. Thiele, K. Arzenbacher, T. Gissibl, H. Giessen, and A. M. Herkommer, Sci. Adv. **3**, e1602655 (2017).
9. S. Schmidt, S. Thiele, A. Toulouse, C. Bösel, T. Tiess, A. Herkommer, H. Gross, and H. Giessen, Optica **7**, 1279 (2020).
10. B. Chen, D. Claus, D. Russ, and M. R. Nizami, Opt. Lett. **45**, 5583 (2020).
11. T. Gissibl, S. Thiele, A. Herkommer, and H. Giessen, Nat. Photonics **10**, 554 (2016).
12. M. Schmid, S. Thiele, A. Herkommer, and H. Giessen, Opt. Lett. **43**, 5837 (2018).
13. M. Schmid, F. Sterl, S. Thiele, A. Herkommer, and H. Giessen, Opt. Lett. **46**, 2485 (2021).
14. A. Bauhofer, "Multiscale Effects of Photochemical Shrinkage in Direct Laser Writing," Ph. D. thesis (ETH Zurich, 2019).
15. H. Ade, R. Toledo-Crow, M. Vaez-Iravani, and R. J. Spontak, Langmuir **12**, 231 (1996).
16. M. Shribak and R. Oldenbourg, Appl. Opt. **42**, 3009 (2003).
17. R. Oldenbourg and G. Mei, J. Microsc. **180**, 140 (1995).
18. M. Ryu, R. Honda, A. Balčytis, J. Vongsvivut, M. J. Tobin, S. Juodkazis, and J. Morikawa, Nanoscale Horiz. **4**, 1443 (2019).
19. S. Ristok, S. Thiele, A. Toulouse, A. M. Herkommer, and H. Giessen, Opt. Mater. Express **10**, 2370 (2020).
20. J. Purtov, A. Verch, P. Rogin, and R. Hensel, Microelectron. Eng. **194**, 45 (2018).
21. E. D. Lemma, F. Rizzi, T. Dattoma, B. Spagnolo, L. Sileo, A. Qualtieri, M. De Vittorio, and F. Pisanello, IEEE Trans. Nanotechnol. **16**, 1 (2016).